agronomy

MDPI

Article

Transformation of Divalent Manganese at Humic Acid–Calcite–Bacteria Interfaces: Kinetics, Thermodynamics, and Mechanisms

Linkui Fan [1,2,3,4], Hongru Guo [1,2,3], Ruyue Liu [1,2,3], Sandres Sikhumbuzo Tshuma [1,2,3], Ting Wang [5], Yan Dou [1,2,3,*], Giuseppe Mele [4] and Guoqiang Gan [1,2,3]

1 School of Water and Environment, Chang'an University, Xi'an 710054, China; a2019900389@163.com (L.F.); 2024129041@chd.edu.cn (H.G.); 2024129071@chd.edu.cn (R.L.); sdumosandres@gmail.com (S.S.T.); ganguoqiang@chd.edu.cn (G.G.)
2 Key Laboratory of Subsurface Hydrology and Ecological Effect in Arid Region of the Ministry of Education, Chang'an University, Xi'an 710054, China
3 Key Laboratory of Eco-Hydrology and Water Security in Arid and Semi-Arid Regions of Ministry of Water Resources, Chang'an University, Xi'an 710054, China
4 Department of Engineering for Innovation, University of Salento, 73100 Lecce, Italy; giuseppe.mele@unisalento.it
5 Shaanxi Environmental Monitoring Center, Xi'an 710054, China; wang_tingp@163.com
* Correspondence: douyan@chd.edu.cn

Abstract

The immobilization and transformation of manganese in soil environments primarily depend on its interactions with soil mineral components, organic matter, and microorganisms. To investigate the migration and transformation of manganese in the water–soil system of loess regions, we used quartz sand (SiO_2) and calcite ($CaCO_3$)—the main components of loess—as soil matrices, along with humic acid (HA) and a typical bacterium (*Bacillus subtilis*) as influencing factors. Laboratory experiments combined with instrumental characterization were employed to examine Mn transformation. The results indicate that the presence of humic acid and bacteria significantly inhibits the cation exchange reaction between Mn and Ca in calcite while enhancing the binding of Mn to organic functional groups (–OH and –COOH). In particular, biofilms formed by bacteria and their metabolites exhibited a more pronounced inhibitory effect on cation exchange and promoted Mn oxidation. The effects of pH and temperature were more evident in the composite systems (quartz sand–calcite–humic acid (QS-CL-HA) and quartz sand–calcite–humic acid–*Bacillus subtilis* (QS-CL-HA-*B.S.*)). Our thermodynamic results show that the transformation of Mn^{2+} in the composite systems best fits the pseudo-second-order kinetic model (chemical adsorption) and the Freundlich model (monolayer adsorption). The values of ΔH (15.22, 5.29 kJ·mol^{-1}) and ΔG (0.82–2.76 kJ·mol^{-1}) confirm that the transformation of Mn^{2+} in these composite systems is non-spontaneous and endothermic. This study demonstrates that, in addition to the effects of minerals, trace organic matter and microorganisms in soil significantly influence the transformation of metallic Mn. The findings also provide a theoretical basis for designing bio-enhanced soil remediation strategies.

Keywords: manganese; loess; calcite; humic acid; *Bacillus subtilis*

Academic Editors: Claudia Campillo-Cora, Antía Gómez-Armesto and Huashou Li

Received: 7 December 2025
Revised: 6 February 2026
Accepted: 13 February 2026
Published: 16 February 2026

1. Introduction

The Loess Plateau in Northwestern China is an important ecological barrier and agricultural area. Loess, due to its unique physicochemical properties (such as high porosity

and strong adsorption), occupies a significant position in agricultural production and engineering construction [1]. However, due to its high soil porosity and low organic matter content, it is prone to the accumulation and migration of heavy metals [2,3]. Manganese (Mn) is an essential micronutrient for both plants and microorganisms; however, elevated concentrations can lead to environmental contamination and pose risks to ecosystems and human health. In China, extensive mining activity has resulted in significant Mn pollution in soils [4,5]. Many of China's loess areas have been reported to be highly contaminated with Mn, adversely affecting soil quality and crop safety [6–8].

Loess is primarily composed of silt-sized particles, with quartz and calcite being the dominant minerals. Quartz, accounting for up to 65% of the mineral content of Loess, is chemically inert but contributes to the soil's physical structure [9,10]. Research has shown that the adsorption mechanism of quartz sand mainly involves weak electrostatic interactions between surface hydroxyl groups and heavy metal ions [11], and calcite's reactivity allows it to interact with metal ions, including Mn^{2+}, through processes such as adsorption and co-precipitation [12]. These interactions can influence the speciation, mobility, and bioavailability of Mn in soils. At the same time, a study by Cui et al. showed that the adsorption of heavy metals by calcite was significantly affected by pH [13]. Understanding the specific roles of calcite and quartz in Mn dynamics is essential for predicting the fate of Mn in loess environments [14].

Humic substances, particularly humic acid (HA), are significant components of soil organic matter and have a profound impact on the behavior of heavy metals [15–17]. HA contains various functional groups capable of binding metal ions, thereby affecting their solubility and mobility. Recent studies have demonstrated that HA can effectively reduce the bioavailability of heavy metals such as cadmium, copper, and lead in contaminated soils [18–22].

Soil microorganisms also play a pivotal role in the transformation of heavy metals [23]. Certain bacteria, such as *Bacillus subtilis*, are putatively involved in altering the oxidation states of metals, thereby influencing their mobility and environmental fate [24–26]. However, the interfacial coupling between humic acid (HA), minerals, and microbial communities is highly complex. Additionally, HA can modulate microbes' physiological activity and community structures [27,28], in turn impacting metal transformation processes [29]. The mechanisms underlying the microbially mediated formation of manganese-rich precipitates and their subsequent interaction with HA require further clarification.

The various mineral components and forms of organic matter in loess combine with each other, producing a synergistic effect during the process of heavy metal transformation. Research has indicated that interaction between minerals (such as iron oxides, aluminum oxides, and calcium carbonate) and organic matter (humic acid, polysaccharides, etc.) can significantly enhance heavy metal adsorption/precipitation capacity, thereby combating pollution [5]. There are also synergistic effects among minerals, microorganisms, and organic matter. One study showed that biochar combined with microbial cells could form carbonate or phosphate minerals, enhancing the effective fixation capacity of heavy metals by over 70% [30]. Furthermore, studies have shown that the process of bacteria facilitating $CaCO_3$ precipitation through pathways such as urea hydrolysis not only enhances soil structure but also leads to co-precipitation of heavy metal ions, thereby promoting the formation of stable mineral phases in the soil [31].

The aim of this study is to investigate the kinetics, thermodynamic adsorption behaviors, and interfacial processes of Mn^{2+} within complex soil environments. To simulate the multi-phase nature of typical loess, we selected calcite, humic acid (HA), and *Bacillus subtilis* as surrogates to represent the dominant mineral, organic, and microbial constituents, respectively. The physicochemical characteristics, putative transformation mechanisms,

and synergistic effects occurring within the ternary calcite–HA–bacteria (CL-HA-*B.S.*) composites were systematically evaluated. This approach fosters a mechanistic understanding of how these representative components collectively influence the sequestration and fate of Mn^{2+} in loess-associated systems.

2. Materials and Methods

2.1. Materials

All chemical reagents utilized in this study were of analytical grade and used without further purification. To simulate the complex multi-phase system of typical loess, calcite, humic acid (HA), and Bacillus subtilis (*B.S.*) were employed as surrogates representing the mineral, organic, and microbial phases, respectively.

Quartz Sand (QS): Analytical grade SiO_2 (purity $\geq$ 99.9%) was ground and sieved through a 100-mesh screen. The particles were washed repeatedly with deionized water until a neutral pH (6.0–7.0) was achieved; this process was followed by drying at 105 °C.

Mineral Surrogate (CL): Natural calcite ($CaCO_3$) was ground and sieved to a particle size of 100–200 mesh. To remove surface contaminants, the particles were subjected to ultrasonic cleaning in deionized water for 30 min and subsequently dried.

Organic Surrogate (HA): Humic acid was purified via dissolution in ultra-pure water (pH 7.4), followed by centrifugation (6000 r/min, 5 min) and filtration through a 0.45 μm membrane to eliminate insoluble impurities. The purified HA was dried at 60 °C for 24 h prior to use [32].

Microbial Surrogate (*B.S.*): B. subtilis (ATCC 6051, Shanghai baocang Microorganisms Center, Shanghai, China) was cultured in Luria–Bertani (LB, BAISIYIJI, Zhongshan, China) liquid medium at 37 °C with continuous aeration. Cells were harvested at the late-logarithmic growth phase ($OD_{600} \approx 1.0$) via centrifugation. The biomass was washed three times with sterile phosphate-buffered saline (PBS, pH 7.4) before experimental application [33,34].

2.2. Preparation of the Composites

The composites were formulated such that they mimicked the typical composition of loess [35,36].

Ternary organic composites (QS-CL-HA) were prepared by mixing QS, CL, and HA in a mass ratio of 10:9:1.

Ternary microbial composites (QS-CL-*B.S.*) were created by adding 1 mL of B. subtilis suspension ($OD_{600} \approx 1.0$) to a 1:1 mixture of QS and CL (2 g total).

Quaternary composites (QS-CL-HA-*B.S.*) were obtained by blending 1.0 g of QS, 0.9 g of CL, and 0.1 g of HA, supplemented with 1 mL of B. subtilis suspension. All composites were used directly in adsorption experiments without further washing.

2.3. Batch Experiments

Batch experiments were performed to evaluate the adsorption behavior of Mn^{2+} on individual components and their respective composites. For each experimental run, 2.0 g of solid material (or 1 mL of bacterial suspension) was introduced into 50 mL polypropylene tubes. After the designated reaction time had elapsed, the suspensions were centrifuged (6000 r/min, 5 min) and filtered (0.45 μm). The concentrations of Mn^{2+} and Ca^{2+} in the supernatant were quantified using Atomic Absorption Spectrometry (AAS). The solid residues were dried at 50 °C and stored at 4 °C for subsequent characterization.

Isotherm Studies: At this stage, 40 mL of Mn^{2+} solutions (5–200 mg/L) were equilibrated with the composites for 24 h at room temperature to determine adsorption capacity.

Effect of pH: The influence of pH (range 2.0–8.0) was investigated using 50 mg/L Mn^{2+} solutions, with the initial pH adjusted using negligible volumes of 0.1 M HCl or NaOH.

Thermodynamic Studies: Experiments were conducted at 20, 30, 40, and 50 °C using 50 mg/L Mn^{2+} solutions to calculate thermodynamic parameters (ΔG, ΔH, and ΔS).

Kinetic Studies: To assess the adsorption rates and putative transformation processes, contact time was varied. Biota-free systems were sampled at intervals of up to 24 h, while bacterium-containing systems were monitored for up to 120 h to capture long-term biological effects.

2.4. Characterization

Functional groups and interfacial coupling mechanisms were analyzed via Fourier Transform Infrared Spectroscopy (FTIR). Crystalline structures and putative newly formed mineral phases were identified using X-ray Diffraction (XRD). The surface morphologies of the surrogates and composites before and after Mn^{2+} sequestration were observed using Scanning Electron Microscopy (SEM).

3. Results and Discussion

3.1. The Results of Batch Experiments

3.1.1. The Effect of the Initial Mn^{2+} Solution

The adsorption capacities of the different components at different concentrations are shown in Figure 1a. All experiments included three parallel groups, and the experimental data in the figure represent the average values of these three parallel groups. The amount of adsorption increased with the increase in the initial concentration for all adsorbents, among which QS had lower adsorption for Mn. The adsorption capacities of the other five adsorbents showed different adsorption effects as the initial Mn concentration increased. At low concentrations (10–50 mg/L), all five adsorbents had high adsorption rates. At a concentration of 50 mg/L, the amounts of Mn^{2+} adsorbed for different adsorbents were distributed as follows: CL > HA > QS-CL-HA-*B.S.* > QS-CL-*B.S.* > QS-CL-HA > QS. When the concentration was 50–200 mg/L, the adsorption amount for each adsorbent continued to increase. At a concentration of 100 mg/L, the adsorption amount for each adsorbent was distributed as follows: QS-CL-HA-*B.S.* > CL > QS-CL-HA > HA > QS-CL-*B.S.* > QS. At a concentration of 200 mg/L, the adsorption amount for each adsorbent corresponded to the following order: HA > QS-CL-HA-*B.S.* > QS-CL-HA > CL > QS-CL-*B.S.* For individual materials, the amount adsorbed by HA was lower than that adsorbed by CL at low concentrations but higher than that adsorbed by CL at high concentrations. QS exhibited the lowest adsorption capacity at any concentration. For the combination of multiple materials, the composites containing HA had a greater adsorption capacity at high concentrations, while the opposite was true of the composites containing *B.S.* When HA and *B.S.* coexist, there is a high adsorption capacity at any concentration, and it is less affected by the original concentration.

3.1.2. Effect of pH

The results of the pH experiments are shown in Figure 1b. Overall, the adsorption rates of Mn^{2+} for the different models in solutions with varying pH levels rank as follows: HA > QS-CL-HA-*B.S* > QS-CL-*B.S* ≈ CL > QS-CL-HA > QS. Notably, they increase with an increase in pH. The adsorption trend for HA is different from the other models, remaining stable at a pH of 5. At pH = 2–4, the adsorption capacity of all the adsorbents was low. HA's adsorption capacity increased significantly at pH = 3–4, while there was a slight decrease for the other models. At pH = 5–7, the adsorption capacity of HA remained almost

unchanged, while the adsorption capacities of the other adsorbents increased slowly. At pH = 7–8, adsorption capacity increased significantly.

Under acidic conditions, in the solution with a pH value of 2–4, H^+ competes with Mn^{2+} for adsorption sites, inhibiting electrostatic adsorption; at the same time, calcite partially dissolves under acidic conditions, releasing Ca^{2+} and thus promoting ion exchange [32,33]. Under neutral conditions, HA is deprotonated (pKa ≈ 4–5), and -COO- engages in electrostatic complexation with Mn^{2+}, so the amount of adsorption increases greatly [34]. Under weakly alkaline conditions, Mn^{2+} is more likely to form basic precipitates, thereby resulting in increased apparent adsorption [35].

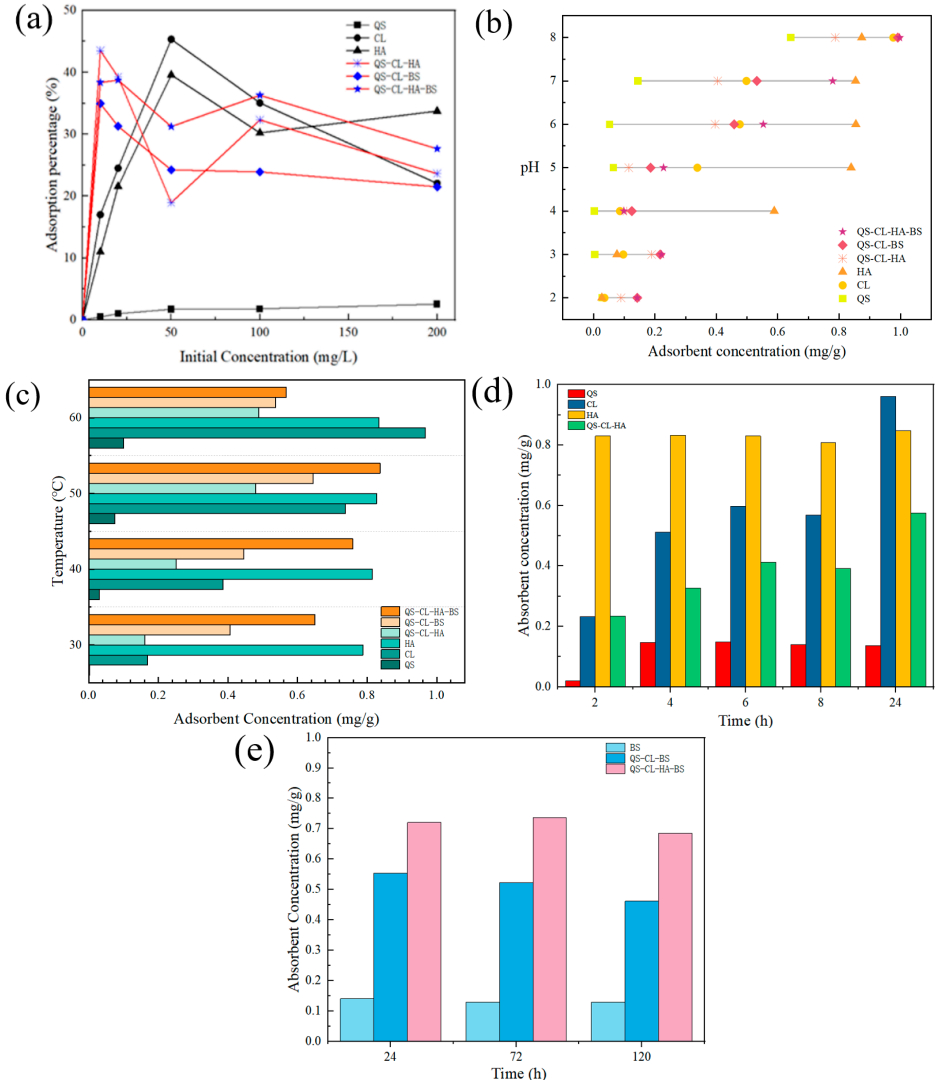

Figure 1. (**a**) Adsorption of different adsorbents at different initial concentrations. (**b**) Adsorption of different components at different pH levels. (**c**) Adsorption of different components at different temperatures. (**d**) Adsorption of different bacteria-free components at different times. (**e**) Adsorption of different bacterial components at different times.

3.1.3. Effect of Temperature

Temperature results are shown in Figure 1c. The QS and HA adsorbents are not greatly affected by temperature. At 30–40 °C, the adsorption capacities of the different adsorbents rank as follows: HA > QS-CL-HA-*B.S.* > QS-CL-*B.S.* > CL > QS-CL-HA > QS. At 40–50 °C, the adsorption capacity of each adsorbent increased with the increase in temperature, with that of CL increasing the most. At 50–60 °C, the adsorption capacity of CL continued to increase with the increase in temperature, the adsorption capacity of QS-CL-HA re-

mained almost unchanged, and the adsorption capacities of the two composites containing *B.S.* decreased.

3.1.4. Effect of Time

Since there is a large gap in time between the system containing bacteria and the system without bacteria, they are discussed separately in this section. For the system without bacteria, the adsorption times were set to 2 h, 4 h, 6 h, 8 h, and 24 h, and the results are shown in Figure 1d below. The adsorption capacity of HA hardly changes with time, indicating that the adsorption equilibrium has been reached at 2 h. QS reaches maximum adsorption at 4 h. The adsorption capacities of the CL and QS-CL-HA adsorbents gradually increase from 2 h to 6 h, decrease briefly from 6 h to 8 h, and then continue to increase until 24 h. At 24 h, the adsorption capacities of the adsorbents rank as follows: CL > HA > QS-CL-HA.

For the system containing bacteria, the adsorption times were set to 24 h, 72 h, and 120 h. To aid comparison, a pure *B.S.* component was added to this group of experiments, and the results are shown in Figure 1e. For the pure *B.S.* component, the adsorption amount is low and less affected by time, and the adsorption equilibrium state can be reached within 24 h. For the QS-CL-*B.S.* component, after the maximum adsorption amount was reached at 24 h, adsorption gradually decreased afterwards. After QS-CL-HA-*B.S.* reached the maximum adsorption amount at 72 h, adsorption also started to decrease. After reaching adsorption equilibrium, the equilibrium adsorption amount for QS-CL-HA-*B.S.* was greater than that for QS-CL-*B.S.*

At low concentrations, adsorption is dominated by surface active sites (such as Ca^{2+} in calcite, -COOH in HA, etc.); at high concentrations, the complexing ability of HA in the mixed system and the extracellular polymers (EPSs) secreted by bacteria provide additional binding sites, and the adsorption capacity is superior. At the same time, the cell wall polysaccharides and peptidoglycans of *Bacillus subtilis* have limited complexing ability for Mn^{2+}, and the binding sites are saturated at high concentrations. *Bacillus subtilis* is most active under neutral conditions and secretes more extracellular polymers (EPSs), enhancing its adsorption performance. Therefore, the adsorption capacities of components containing *B.S.* under neutral conditions will be slightly higher than those of other components [36]. Bacterial activity is inhibited under alkaline conditions, and the contribution of biological adsorption is reduced [37,38]. The influence of temperature (20–50 °C) indicates that the sequestration of Mn^{2+} is an endothermic process, where elevated temperatures enhance molecular diffusion and the thermal activation of surface functional groups. While the metabolic activity of *B.S.* typically peaks near its optimal growth temperature (approx. 37 °C), the continued increase in Mn^{2+} removal at 50 °C suggests a synergistic effect. The endothermic nature of the interaction drives increased Mn^{2+} complexation with calcite and HA. Although metabolic activity may be constrained at 50 °C, the Extracellular Polymeric Substances (EPS) and cell-wall functional groups (e.g., carboxyl and phosphoryl groups) serve as thermally stable templates for Mn^{2+} biosorption and indirect biomineralization. This transition from active biological regulation to a combined thermally driven physicochemical and passive biosorption mechanism explains the enhanced efficiency at higher temperatures. For components without bacteria, adsorption equilibrium can be reached relatively quickly. After reaching adsorption equilibrium, some heavy metal ions may be desorbed, resulting in a slight decrease in adsorption capacity. As adsorption continues, the internal structure of CL changes, some active sites are activated, and the amount adsorbed begins to gradually increase. For components containing bacteria, with longer-term adsorption, the physiological activity of bacteria has a greater impact on the amount adsorbed. As adsorption proceeds, the active sites on the surfaces of bacteria are gradually filled,

resulting in a decrease in the physiological activity of the bacteria, and less EPS is secreted, resulting in a decrease in adsorption.

3.2. Analysis of the Characterization Results

3.2.1. FTIR

FTIR was performed on QS, QS-CL-HA, and QS-CL-HA-*B.S.* before and after adsorption, and the results are shown in Figure 2a. Regarding QS, pure quartz sand only has weak absorption peaks at around 830 and 610 cm^{-1}, which are due to Si-O-Si bending vibrations and Si-O lattice vibrations, respectively. There was no obvious change in the spectrum before or after adsorption, indicating that adsorption of the heavy metal Mn^{2+} only occurs on the surface of QS, no significant chemical changes occur, and the structure is not determined or destroyed. Regarding the QS-CL-HA composite, after CL and HA were added, obvious absorption peaks appeared at 3430 and 1620 cm^{-1}, which were attributed to the stretching vibration of -OH and -NH and the bending of C=O, C=C, or N-H, respectively, indicating that there were numerous polar groups in HA, and there were also some double bonds or aromatic groups in CL and HA. Compared with that before adsorption, the peak at 3430 cm^{-1} after adsorption became narrower, indicating that -OH or -COOH is complexed with Mn^{2+}, and the interaction between the organic phase and the inorganic phase is enhanced [39]. The curve after adsorption is smoother overall, indicating that the surface is denser and the molecular arrangement is more orderly. We now turn to the QS-CL-HA-*B.S.* composite. *B.S.* is a common soil microorganism, and its metabolites contain a variety of organic components such as proteins, polysaccharides, and lipids. Characteristic absorption will also appear around 3400 cm^{-1} and 1650 cm^{-1}, but the absorption peak at 3430 cm^{-1} weakened after *B.S.* was added. This is because the extracellular polymer EPS secreted by *B.S.* contains numerous -OH and $-NH_2$ groups in its protein, polysaccharide, and nucleic acid components; these groups can be strongly combined with polar groups in minerals or humic acid through hydrogen bonds, resulting in a weakening of the absorption peak. The curve after adsorption also becomes smoother [40].

FTIR analysis revealed that the addition of HA and *B.S.* changed the surface functional groups of quartz sand and calcite through various mechanisms, such as hydrogen bonding, coordination complexation, and metabolite adsorption, resulting in significant changes in the intensity, width, and position of each typical peak. At the same time, when multiple components coexist, the absorption peaks of each component overlap and compete with each other, making the typical mineral peaks (such as Si-O and CO_3^{-}) and organic peaks (such as C-O, C=O, and O-H) appear in the spectrum as a comprehensive effect of position shift and intensity change. A more detailed exploration of the adsorption mechanism of each component requires further characterization results for analysis and validation [41].

3.2.2. XRD

XRD analysis was performed on QS, QS-CL-HA, and QS-CL-HA-*B.S.* before and after adsorption, yielding the spectra shown in Figure 2b. Evidently, only quartz peaks appear in the bottom layer of the QS spectrum. In the second layer of QS-CL-HA, the calcium calcite peak at about 29.4° can clearly be seen, indicating that the system already contains the CL phase. HA itself has no long-range-ordered lattice. In the spectrum of the QS-CL-HA composite, no new sharp peaks appear in the low-angle region except for the QS and CL peaks, indicating that has HA maintained an amorphous distribution [42]. After the introduction of *B.S.*, the background broad peak in the low-angle region increased, indicating that the cell organic matter of *B.S.* was filled or adsorbed onto the surface of the entire system. At the same time, its extracellular polymer complexed Ca^{2+} with the cell surface in large quantities and provoked the stable amorphous calcium carbonate to

polymerize and form precipitation, thereby inhibiting or shielding the crystal distribution of calcite crystals, causing the diffraction peak at 29.4° to disappear [43]. After adsorption, the peak at 29.4° in the spectrum of the QS-CL-HA composite shifted position because of the decrease in interplanar spacing after Mn^{2+} partially replaced Ca^{2+}. At the same time, no peaks, such as those corresponding to MnO_2 (36°) or $MnCO_3$ (32°), were observed in the 25–40° range, proving that the metal mainly exists in the form of a solid solution and undergoes surface coordination rather than precipitating an independent crystalline phase [44]. For QS-CL-HA-*B.S.*, the introduction of Mn^{2+} after adsorption caused lattice distortion, which led to the coverage of the QS surface and the disappearance of the quartz diffraction peaks at 20.8° and 26.6°. The baseline is elevated in the 10–25° region, indicating that some amorphous calcium carbonate (AAC) precursors formed under the action of the EPS. AAC has no long-range-ordered structure, so a scattering background was generated in this area. Subsequently, *B.S.* and EPS form a multilayer organic film on the surface of the system, stabilizing the AAC precursor, raising the broad peak background in the low-angle region, and generating a new diffraction peak at 29° [45,46].

XRD analysis showed that QS, as an inert substrate, exhibited no significant changes in its diffraction peak and hardly participated in the adsorption of Mn^{2+}. CL will fix Mn^{2+} via lattice solid solution and growth inhibition, manifested as 26.6° and 29.4° peak position shifts and intensity and width changes. HA appears in the form of an amorphous organic layer, and XRD only shows a broad baseline rise. Additionally, its -COO^- and -OH- sites enhance the fixation of Mn^{2+} through complexation. *B.S.* and EPS not only stabilize the amorphous calcium carbonate precursor but also guide the directional growth of the crystal nucleus, and the low-angle wide peak and high-angle peak are further enhanced. Under the synergistic effect of HA and *B.S.*, Mn^{2+} is not only embedded in the calcite lattice but also fixed by organic biomacromolecules in a coordinated amorphous state [47,48].

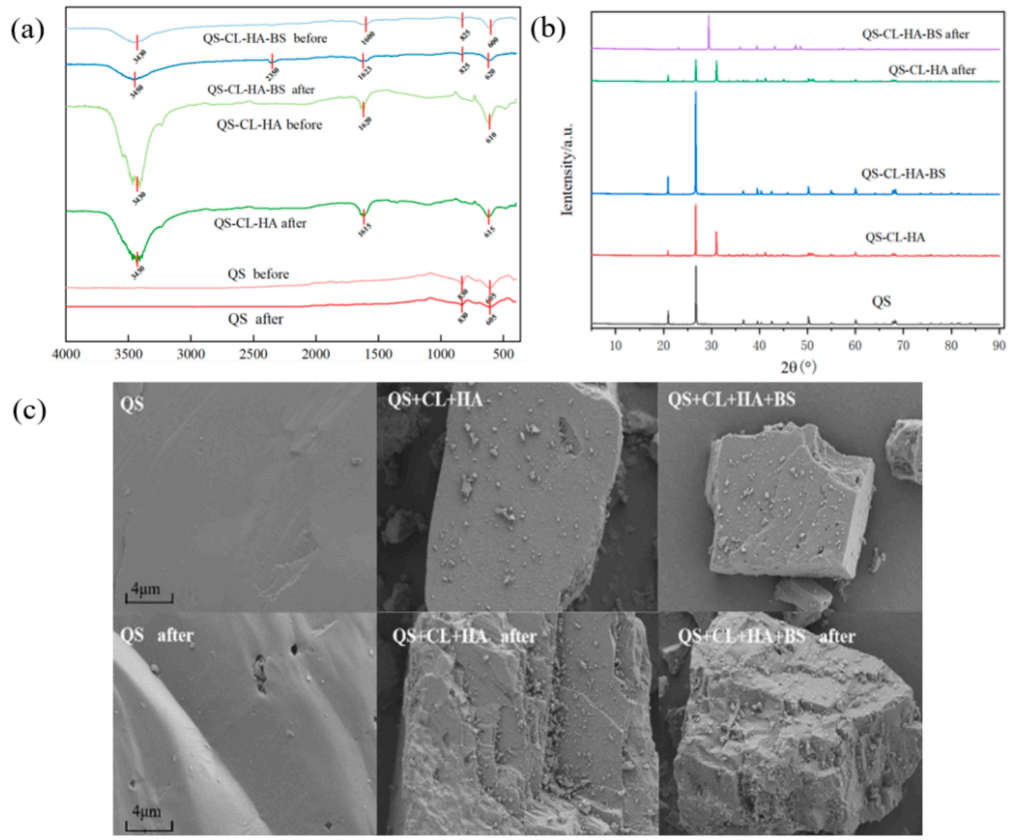

Figure 2. (**a**) FTIR Spectrum. (**b**) XRD Spectrum. (**c**) SEM images of different components before and after adsorption.

3.2.3. SEM

Morphological images of QS, QS-CL-HA, and QS-CL-HA-*B.S.* before and after adsorption are shown in Figure 2c. The SEM images reveal that the surface of QS before adsorption is relatively smooth. After CL and HA were added, a large number of fine particles and clusters appeared on the surface of the QS, exhibiting an obvious granular, rough structure, indicating that CL and HA were aggregated or attached to its surface. The surface of the system containing *B.S.* is more irregular, and bacterial colonies and organic films formed by EPS on the surface of the material are readily evident. At the same time, there are more biological components such as surface proteoglycans, further improving particle attachment density and heterogeneity. After adsorption, the SEM images reveal the deposition characteristics of and structural changes to the surfaces of the components. There are no obvious changes in the surface characteristics of the QS after adsorption, indicating that the adsorption effect of the pure QS component with respect to Mn^{2+} is weak, while in the system containing CL, a small quantity of fine particles appeared on the surface after adsorption. These coatings may be a result of the precipitation of manganese oxide (MnO_2) or manganese carbonate ($MnCO_3$). Pourahmad et al. have shown that layers containing Mn can form on the surface of calcite, of which about 5% is Mn oxide [49]. In addition, the adsorbed QS-CL-HA composites formed a denser deposition layer on the basis of the original surface particles, and more fine particles covered the surface, indicating that a denser manganese deposition layer formed on the surface of the composite system, blocking the original micropores and improving the retention and enrichment of manganese ions [50]. However, the particle distribution of the component containing *B.S.* after adsorption is more complicated, and the surface shows multiple cracks and peeling layers, which were generated by the continuous accumulation of manganese oxides and biofilm formation, resulting in the peeling of the substrate [45,51].

In addition, the pore-blocking phenomenon is more obvious in the composite material. After adsorption, fine sediments could be seen filling the original particle gaps, causing the surface to display more continuous agglomerates rather than the original porous structure, indicating that the microscopic pores were closed by the manganese deposition layer. This is consistent with the phenomenon wherein the calcite surface is covered by a manganese oxide layer, which hinders further dissolution and material transfer. In humic-acid-containing composites, humic acid itself may also participate in the formation of an organic–inorganic composite deposition layer, causing the surface to present more layers and particle agglomeration structures. As shown in the figure, the QS-CL-HA sample exhibited denser particle coverage after adsorption than before adsorption, indicating that humic acid promoted the complexation and precipitation of manganese on the surface. On the one hand, *B.S.* provides additional biological adsorption sites (EPS and cell wall combination), which will capture and deposit a portion of Mn^{2+} [52] On the other hand, the strain has the ability to oxidize Mn, as its microbial activity induces the precipitation of manganese-containing mineral phases, further promoting surface deposition. The addition of *B.S.* not only makes the surface attachment structure more complex but also may promote the formation of a bio-mineral composite deposition layer.

3.3. Models

3.3.1. Kinetics Model

The pseudo-first-order and pseudo-second-order kinetic models were used to study the adsorption kinetics of the QS-CL-HA component without bacteria, as shown in Figure 3a. According to the calculations, the R^2 values of the pseudo-first-order and pseudo-second-order kinetic models are both above 0.9, and both have a strong correlation, indicating that in the QS-CL-HA system, physical adsorption and chemical adsorption

occur at the same time, but the R^2 of the pseudo-second-order kinetic curve is larger (i.e., it is better than the pseudo-first-order kinetic curve), indicating that chemical adsorption is dominant in this system. In general, the adsorption of QS-CL-HA is a multi-step mass transfer controlled process, which predominantly consists of film diffusion or surface chemical adsorption in the early stage and turns into intraparticle diffusion and chemical coupling in the middle and late stages [53].

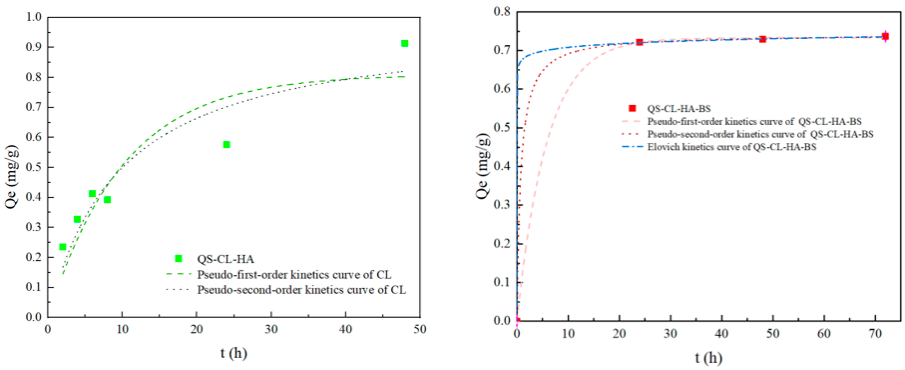

(**a**) (**b**)

Figure 3. Kinetic adsorption models of the (**a**) QS-CL-HA and (**b**) QS-CL-HA-*B.S.* systems.

The adsorption kinetics of the components of QS-CL-HA-*B.S.*, containing bacteria, were studied using pseudo-first-order, pseudo-second-order, and Elovich kinetic models, as shown in Figure 3b. According to the calculations, the R^2 of the Elovich model can reach 0.99999, indicating that adsorption is significantly affected by surface heterogeneity in this case. The fitting parameters are better in the presence of bacteria. Although this heterogeneity is partly due to the complex chemical composition at the soil–microbe interface, considering the physiological responses of microbes under heavy metal stress (such as EPS secretion). Detailed calculation procedures for kinetics models are provided in the Supplementary Information (S1).

3.3.2. Thermodynamic Model

An isothermal adsorption model was established for the QS-CL-HA system, and the Langmuir and Freundlich isothermal adsorption models were used for calculation. The formula for the Langmuir model is $Q_e = \frac{Q_m K_L C_e}{1+K_L C_e}$, where K_L (L/mg) is the Langmuir constant, which is related to adsorption energy/affinity. The formula for the Freundlich model is $Q_e = K_F C^{1/n}$, where K_F [(mg/g)(L/mg)^(1/n)] is the Freundlich constant, representing an indicator of adsorption capacity.

The results are shown in Figure 4a. According to the results, the isothermal adsorption of the QS-CL-HA system is more consistent with the Freundlich model. The steep initial slope reaction system has a high affinity for low-concentration Mn^{2+}, a phenomenon that can mainly be attributed to the strong complexation of HA and the ion exchange of CL. In the high-concentration region, Q_e continues to rise, indicating that the CL-HA complex can continue to adsorb through physical accumulation or surface precipitation; at the same time, the growth rate of Q_e decreases, indicating that the active sites tend to be saturated, and the maximum amount of adsorption is determined by the number of chemical sites possessed by HA and CL [54,55].

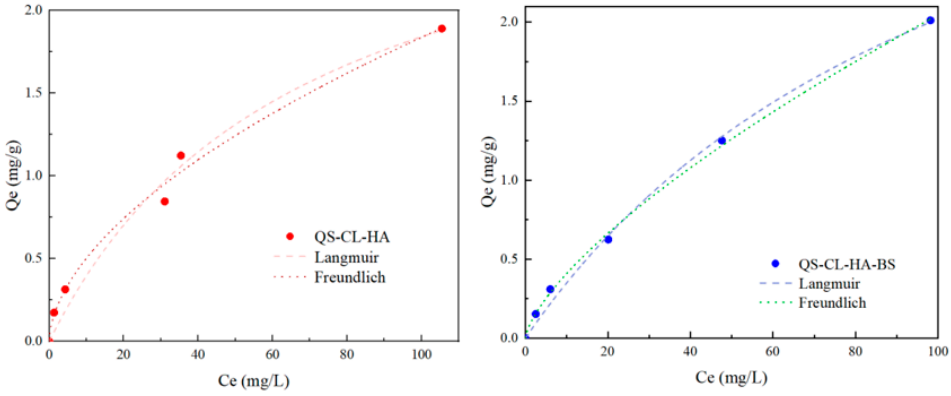

Figure 4. (**a**) Isotherm adsorption models of the QS-CL-HA-*B.S.* system. (**b**) Isotherm adsorption models of the QS-CL-HA-*B.S.* system.

The QS-CL-HA-*B.S.* system was also analyzed using the Langmuir and Freundlich isothermal adsorption models, as shown in Figure 4b. According to the model calculation results, the isothermal adsorption process of the composite system is more consistent with the Freundlich model. In the low-concentration area, the negatively charged groups in EPS quickly adsorb Mn^{2+} through electrostatic attraction, and the growth rate slows down in the high-concentration area. At this time, Mn^{2+} attaches to the surface of the biofilm, generating multi-layer adsorption, and the maximum amount of adsorption is determined by the number of chemical sites *B.S.* and HA possess [56,57]. Detailed calculation procedures for adsorption capacity and thermodynamic parameters are provided in the Supplementary Information (S2–S3).

According to the calculations in the table, the adsorption processes of the two QS-CL-HA and QS-CL-HA-*B.S.* systems between 30 °C and 60 °C in terms of adsorption and desorption are on the verge of dynamic equilibrium. The ΔG value is slightly positive and close to zero, indicating that this adsorption process is in a thermodynamically metastable state, reflecting a high degree of reversibility and environmental sensitivity between the microbial surface and heavy metal ions [58]. The thermodynamic parameters were re-evaluated using the dimensionless equilibrium constant K to ensure physical consistency with the observed spontaneous adsorption. Within the temperature range of 303–333 K, ΔG gradually decreases with increasing temperature, indicating that this adsorption process is significantly influenced by temperature. The positive value of ΔH indicates the endothermic nature of the adsorption, suggesting that higher temperatures provide the necessary energy to overcome the activation barrier for chemical bond formation or ion exchange. Furthermore, the positive value of ΔS is the key driving force for the reaction. This increase in entropy is attributed to the release of hydrated water molecules from the Mn^{2+} ions and the surrogate surfaces into the bulk solution upon adsorption, which increases the overall disorder of the system. Therefore, the adsorption process is entropy-driven, as the TΔS term effectively offsets the endothermic enthalpy change, resulting in a spontaneous ΔG.

This 'weak spontaneity' or 'near-equilibrium' state suggests that microorganisms' interception of heavy metals may not be a strong 'permanent chemical bond' but rather a biophysical buffering effect [59].

3.4. Mechanism Discussion

The transformation of manganese in different systems involves the synergistic effects of physicochemical and biological processes, and the experimental and characterization results reveal these mechanisms, as shown in Figure 5. The carboxyl (-COOH) and hy-

droxyl (-OH) groups in humic acid (HA) govern the adsorption of Mn^{2+} through ligand exchange and electrostatic interactions. FTIR analysis showed that the -OH stretching peak (3430 cm^{-1}) narrowed after adsorption, indicating that Mn^{2+} formed inner-layer complexes with deprotonated functional groups under neutral conditions (pH 5–7). The Freundlich isotherm model further supported the multilayer adsorption driven by the heterogeneous binding sites of HA, especially at high Mn^{2+} concentrations. Calcite promoted Mn^{2+} fixation through ion exchange ($Ca^{2+}\leftrightarrow Mn^{2+}$) and coprecipitation. The XRD results show that the calcite diffraction peak (29.4°) shifted after adsorption, indicating that Mn^{2+} partially replaced Ca^{2+} in the lattice. The occurrence of $MnCO_3$ precipitation under alkaline conditions (pH > 7) further enhanced this apparent adsorption capacity. *Bacillus subtilis* improves adsorption performance via secreting extracellular polymers (EPSs) and biomineralization. EPS is rich in polysaccharides and proteins, providing additional binding sites for Mn^{2+} through electrostatic attraction and hydrogen bonding (the 3430 cm^{-1} peak in FTIR is weakened). The SEM images show biofilm formation and surface deposition of an amorphous substance, which can be attributed to microbial oxidation and metabolic activities. The Elovich kinetic model (R^2 = 0.999) highlights the dynamic role of biofilm in heterogeneous adsorption.

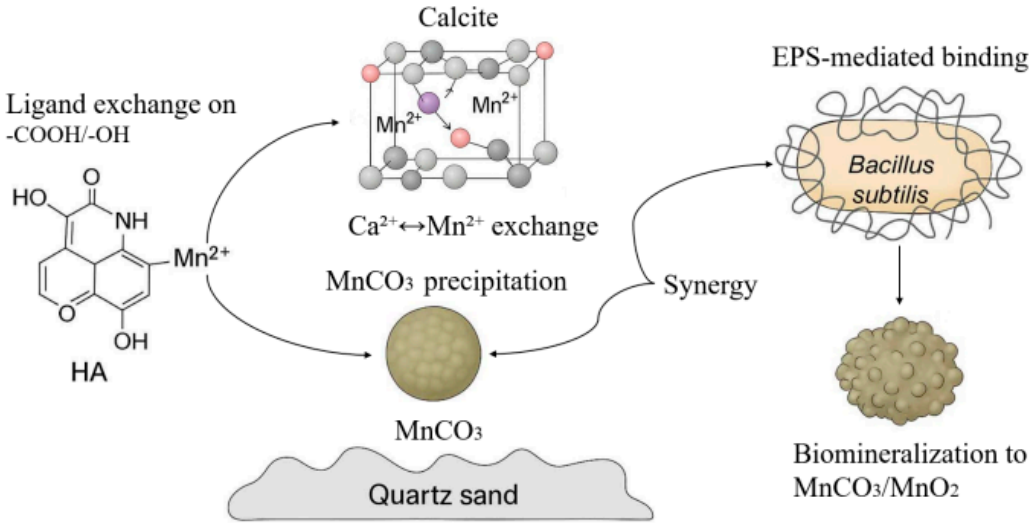

Figure 5. Prediction of the mechanism of action of the mineral–microbe complex system with respect to the metal Mn^{2+}.

The quadruple system QS-CL-HA-*B.S.* exhibited a compound effect, where the organic layer of HA promotes Mn^{2+} complexation, calcite provides ion exchange sites, and microorganisms enhance Mn^{2+} retention via stabilizing amorphous phases (such as AAC precursors) and biofilm formation. The SEM results show that the surface of the composite system is more densely aggregated, and the pores are blocked, indicating the synergistic effect of physical retention and chemical binding.

4. Conclusions

In this study, a composite system consisting of key components of loess (quartz sand (QS), calcite (CL), humic acid (HA), and *Bacillus subtilis* (*B.S.*)) was constructed to reveal the mechanism behind the synergistic effect of multiple components on the transformation of Mn^{2+}. Combining the residual ion concentrations detected via atomic absorption spectroscopy (AAS), the characterization results obtained via FTIR, XRD, and SEM, and analysis of the kinetic and isotherm models, we draw the following main conclusions: (1) The HA-based composite system QS-CL-HA reaches its maximum adsorption capacity

at pH 6, which is significantly better than the values for the individual mineral (QS and CL) systems. The QS-CL-HA system is highly sensitive to pH, temperature, and initial concentration. At pH 5–7, HA deprotonation enhances complexation. At 30–50 °C, adsorption is an endothermic process, and biological activity is enhanced. At an initial concentration of 10–200 mg/L, the system's behavior conforms to the Langmuir–Freundlich mixing model, revealing the synergistic effect of multilayer adsorption and surface heterogeneity. The maximum adsorption capacity is determined by the number of chemical sites on HA and CL. In the system containing *B.S.*, *Bacillus subtilis* secreted extracellular polymers (EPSs) to provide additional binding sites and induced Mn^{2+} biomineralization, leading to $MnCO_3$ precipitation, which increased the adsorption capacity of the composite system by 30–40%. Microbial activity reached its peak under neutral conditions, but due to the effect of temperature on bacterial activity, the adsorption performance decreased at temperatures above 60 °C due to protein denaturation and functional-group degradation. (2) FTIR and XRD characterization confirmed that the polar groups (-COOH and -OH) of HA and microbial EPS enhanced Mn^{2+} fixation through hydrogen bonding and coordination complexation. SEM revealed that the microbially mediated biofilm and mineral–organic composite deposition layer significantly changed the surface morphology, inhibited desorption, and improved the Mn^{2+} retention capacity. For various components, QS mainly provides a physical adsorption base; CL fixes Mn^{2+} through Ca^{2+}/Mn^{2+} ion exchange and carbonate precipitation ($MnCO_3$); the carboxyl and phenolic hydroxyl groups of HA have strong coordination and complexing effects on Mn^{2+}; and after the introduction of *B.S.*, bacterial metabolites and extracellular polymers (EPS) provide additional coordination sites and induce biomineralization (amorphous/crystalline manganese carbonate), improving adsorption capacity.

This study clarifies, for the first time, the multi-level mechanism of Mn^{2+} fixation via the synergistic effect of minerals, organic matter, and microorganisms through a simplified soil model system, providing a theoretical basis for the remediation of manganese pollution on the Loess Plateau.

Supplementary Materials: The following supporting information can be downloaded at: https://www.mdpi.com/article/10.3390/agronomy16040462/s1.

Author Contributions: L.F.: Writing—original draft, Methodology, Data curation; H.G.: Formal analysis, Data curation; R.L.: Writing—review and editing, Formal analysis; S.S.T.: Formal analysis, Data curation; T.W.: Supervision, Resources, Funding acquisition; Y.D.: Writing—review and editing, Supervision, Resources, Funding acquisition, Conceptualization; G.M.: Writing—review and editing, Supervision, Resources; G.G.: Writing—review and editing, Supervision. All authors have read and agreed to the published version of the manuscript.

Funding: Supported by (1) Fundamental Research Funds for the Central Universities, CHD. (No. 300102294902 and No. 2024SHEEAR005). (2) Shaanxi Key Environmental Monitoring and Forewarding of Trace Pollutants (No. SHJKFJJ-ZD-202406). During the preparation of this work, the authors used DeepSeek to improve the clarity and accuracy of the article. After using this tool/service, the authors reviewed and edited the content as needed, and they take full responsibility for the content of the published article.

Data Availability Statement: All data supporting the findings of this study are provided within the article and its Electronic Supplementary Information (ESI). No additional datasets were generated or analyzed.

Conflicts of Interest: The authors declare that they have no known competing financial interests or personal relationships that could have appeared to influence the work reported in this paper.

References

1. Liu, Z.; Ma, X.; Zhou, D.; Lu, L.; Zhang, H.; Bai, Y.; Han, H. The geological origins and soil properties of loess-like silty clay: A case study in the jinan area. *Sci. Rep.* **2024**, *14*, 12612. [CrossRef]
2. Meng, Y.; Li, P.; Xiao, L.; Wang, R.; Yang, S.; Han, J.; Hu, B. Heavy Metal Content and Pollution Assessment in Typical Check Dam Sediment in a Watershed of Loess Plateau, China. *Sustainability* **2022**, *14*, 8597. [CrossRef]
3. Guo, Z.; Li, P.; Yang, X.; Wang, Z.; Wu, Y.; Li, G.; Liu, G.; Ritsema, C.J.; Geissen, V.; Xue, S. Effects of Microplastics on the Transport of Soil Dissolved Organic Matter in the Loess Plateau of China. *Environ. Sci. Technol.* **2023**, *57*, 20138–20147. [CrossRef] [PubMed]
4. Wang, N.; Luo, Y.; Liu, Z.; Sun, Y. Spatial distribution characteristics and evaluation of soil pollution in coal mine areas in Loess Plateau of northern Shaanxi. *Sci. Rep.* **2022**, *12*, 16440. [CrossRef]
5. Li, Q.; Wang, Y.; Li, Y.; Li, L.; Tang, M.; Hu, W.; Chen, L.; Ai, S. Speciation of heavy metals in soils and their immobilization at micro-scale interfaces among diverse soil components. *Sci. Total Environ.* **2022**, *825*, 153862. [CrossRef] [PubMed]
6. Li, M.S.; Yang, S.X. Heavy Metal Contamination in Soils and Phytoaccumulation in a Manganese Mine Wasteland, South China. *Air Soil Water Res.* **2008**, *1*, ASWR.S2041. [CrossRef]
7. Liu, K.; Liang, X.; Li, C.; Yu, F.; Li, Y. Nutrient status and pollution levels in five areas around a manganese mine in southern China. *Front. Environ. Sci. Eng.* **2020**, *14*, 100. [CrossRef]
8. Ji, H.; Zhang, J.; Zhao, Y.; Huang, H.; Ma, Y.; Liang, D.; Chen, F.; Huo, H.; Wang, S.; Xie, T. Heavy metal pollution migration and its ecological impact on microbial communities in the karst region of Guangxi. *Sci. Rep.* **2025**, *15*, 14750. [CrossRef]
9. Li, Y.; Shi, W.; Aydin, A.; Beroya-Eitner, M.A.; Gao, G. Loess genesis and worldwide distribution. *Earth Sci. Rev.* **2020**, *201*, 102947. [CrossRef]
10. Drewnik, M.; Skiba, M.; Szymański, W.; Żyła, M. Mineral composition vs. soil forming processes in loess soils—A case study from Kraków (Southern Poland). *Catena* **2014**, *119*, 166–173. [CrossRef]
11. Wang, T.; Cao, W.; Wang, Y.; Qu, C.; Xu, Y.; Li, H. Surface modification of quartz sand: A review of its progress and its effect on heavy metal adsorption. *Ecotoxicol. Environ. Saf.* **2023**, *262*, 115179. [CrossRef]
12. Wang, J.-M.; Zhao, J.; Qin, X.-Z.; Wang, Z. Theoretical study of adsorption mechanism of heavy metals As and Pb on the calcite (104) surface. *Mater. Today Commun.* **2021**, *26*, 101742. [CrossRef]
13. Cui, W.; Li, X.; Duan, W.; Xie, M.; Dong, X. Heavy metal stabilization remediation in polluted soils with stabilizing materials: A review. *Environ. Geochem. Health* **2023**, *45*, 4127–4163. [CrossRef]
14. Xu, P.; Qian, H.; Li, W.; Ren, W.; Yang, F.; Wang, L. New insights into the seepage behavior of heavy metal-contaminated loess and its underlying geochemical mechanism. *J. Hydrol.* **2023**, *620*, 129476. [CrossRef]
15. Zhao, K.; Yang, Y.; Peng, H.; Zhang, L.; Zhou, Y.; Zhang, J.; Du, C.; Liu, J.; Lin, X.; Wang, N. Silicon fertilizers, humic acid and their impact on physicochemical properties, availability and distribution of heavy metals in soil and soil aggregates. *Sci. Total Environ.* **2022**, *822*, 153483. [CrossRef] [PubMed]
16. Wang, Z.; Lu, Q.; Liu, C.; Tian, H.; Wang, J.; Xie, L.; Liu, Q.; Zeng, H. Nanoscale insights into the interaction mechanism underlying the adsorption and retention of heavy metal ions by humic acid. *Environ. Sci. Technol.* **2024**, *58*, 3412–3422. [CrossRef]
17. Amutenya, E.L.; Zhou, F.; Liu, J.; Long, W.; Ma, L.; Liu, M.; Lv, G. Preparation of humic acid-bentonite polymer composite: A heavy metal ion adsorbent. *Heliyon* **2022**, *8*, e09720. [CrossRef] [PubMed]
18. Rong, Q.; Zhong, K.; Huang, H.; Li, C.; Zhang, C.; Nong, X. Humic Acid Reduces the Available Cadmium, Copper, Lead, and Zinc in Soil and Their Uptake by Tobacco. *Appl. Sci.* **2020**, *10*, 1077. [CrossRef]
19. Su, X.; Hu, J.; Zhang, J.; Liu, H.; Yan, C.; Xu, J.; Ma, Y.; Song, J. Investigating the adsorption behavior and mechanisms of insoluble Humic acid/starch composite microspheres for metal ions from water. *Colloids Surf. A Physicochem. Eng. Asp.* **2021**, *610*, 125672. [CrossRef]
20. Fu, Y.; Zhu, Y.; Dong, H.; Li, J.; Zhang, W.; Shao, Y.; Shao, Y. Mechanisms of the effects of humic acid on antibiotic resistance genes and microbial communities in Cd-contaminated soils. *Process Saf. Environ. Prot.* **2022**, *160*, 62–69. [CrossRef]
21. Zhao, Q.; Qiu, Y.; Lan, T.; Li, J.; Li, B.; Wu, Z.; Chen, L.; Liu, R.; Zhou, Y.; Wu, W. Comparison of lead adsorption characteristics onto soil-derived particulate organic matter versus humic acid. *J. Soils Sediments* **2021**, *21*, 2589–2603. [CrossRef]
22. Wang, M.; Song, G.; Zheng, Z.; Mi, X.; Song, Z. Exploring the impact of fulvic acid and humic acid on heavy metal availability to alfalfa in molybdenum contaminated soil. *Sci. Rep.* **2024**, *14*, 32037. [CrossRef] [PubMed]
23. Narayanan, M.; Ma, Y. Mitigation of heavy metal stress in the soil through optimized interaction between plants and microbes. *J. Environ. Manag.* **2023**, *345*, 118732. [CrossRef] [PubMed]
24. Darma, A.; Yang, J.; Bloem, E.; Możdżen, K.; Zandi, P. Arsenic biotransformation and mobilization: The role of bacterial strains and other environmental variables. *Environ. Sci. Pollut. Res.* **2022**, *29*, 1763–1787. [CrossRef]
25. Alotaibi, B.S.; Khan, M.; Shamim, S. Unraveling the underlying heavy metal detoxification mechanisms of *Bacillus* species. *Microorganisms* **2021**, *9*, 1628. [CrossRef]
26. Zhou, W.; Zhu, Y.; Achal, V. Synergistic mechanisms of humic acid and biomineralization in cadmium remediation using *Lysinibacillus fusiformis*. *Environ. Microbiol. Rep.* **2024**, *16*, e70037. [CrossRef]

27. Li, C.; Li, H.; Yao, T.; Su, M.; Ran, F.; Li, J.; He, L.; Chen, X.; Zhang, C.; Qiu, H. Effects of swine manure composting by microbial inoculation: Heavy metal fractions, humic substances, and bacterial community metabolism. *J. Hazard. Mater.* **2021**, *415*, 125559. [CrossRef]
28. Wang, M.; Song, G.; Zheng, Z.; Song, Z.; Mi, X.; Hua, J.; Wang, Z. Effect of humic substances on the fraction of heavy metal and microbial response. *Sci. Rep.* **2024**, *14*, 11206. [CrossRef]
29. Campillo-Cora, C.; Rodríguez-Seijo, A.; Pérez-Rodríguez, P.; Fernández-Calviño, D.; Santás-Miguel, V. Effect of heavy metal pollution on soil microorganisms: Influence of soil physicochemical properties. A systematic review. *Eur. J. Soil Biol.* **2025**, *124*, 103706. [CrossRef]
30. Zhou, Y.; Zhao, X.; Jiang, Y.; Ding, C.; Liu, J.; Zhu, C. Synergistic remediation of lead pollution by biochar combined with phosphate solubilizing bacteria. *Sci. Total Environ.* **2023**, *861*, 160649. [CrossRef]
31. Zhang, Y.; Peng, J.; Wang, Z.; Zhou, F.; Yu, J.; Chi, R.; Xiao, C. Metagenomic analysis revealed the bioremediation mechanism of lead and cadmium contamination by modified biochar synergized with *Bacillus cereus* PSB-2 in phosphate mining wasteland. *Front. Microbiol.* **2025**, *16*, 1529784. [CrossRef] [PubMed]
32. Kim, J.J.; Lee, S.S.; Fenter, P.; Myneni, S.C.B.; Nikitin, V.; Peters, C.A. Carbonate Coprecipitation for Cd and Zn Treatment and Evaluation of Heavy Metal Stability Under Acidic Conditions. *Environ. Sci. Technol.* **2023**, *57*, 3104–3113. [CrossRef]
33. Zhao, W.; Ren, B.; Hursthouse, A.; Jiang, F. The adsorption of Mn(II) by insolubilized humic acid. *Water Sci. Technol.* **2020**, *82*, 747–758. [CrossRef] [PubMed]
34. Liu, L.; Zhang, T.; Yu, X.; Mkandawire, V.; Ma, J.; Li, X. Removal of Fe^{2+} and Mn^{2+} from Polluted Groundwater by Insoluble Humic Acid/Tourmaline Composite Particles. *Materials* **2022**, *15*, 3130. [CrossRef] [PubMed]
35. Wang, H.; Zhu, J.; Fu, Q.; Hu, H. Adsorption of phosphate on pure and humic acid-coated ferrihydrite. *J. Soils Sediments* **2015**, *15*, 1500–1509. [CrossRef]
36. Mikutta, R.; Baumgärtner, A.; Schippers, A.; Haumaier, L.; Guggenberger, G. Extracellular polymeric substances from *Bacillus subtilis* associated with minerals modify the extent and rate of heavy metal sorption. *Environ. Sci. Technol.* **2012**, *46*, 3866–3873. [CrossRef]
37. Maksimova, Y.; Eliseeva, A.; Maksimov, A. Metabolic and Morphological Aspects of Adaptation of Alkaliphilic *Bacillus aequororis* 5-DB and Alkali-Tolerant *Bacillus subtilis* ATCC 6633 to Changes in pH and Mineralization. *Int. J. Microbiol.* **2024**, *2024*, 3087296. [CrossRef]
38. Msimbira, L.A.; Subramanian, S.; Naamala, J.; Antar, M.; Smith, D.L. Secretome Analysis of the Plant Biostimulant Bacteria Strains *Bacillus subtilis* (EB2004S) and *Lactobacillus helveticus* (EL2006H) in Response to pH Changes. *Int. J. Mol. Sci.* **2022**, *23*, 15144. [CrossRef]
39. Reig, F.B.; Adelantado, J.V.; Moya Moreno, M.C. FTIR quantitative analysis of calcium carbonate (calcite) and silica (quartz) mixtures using the constant ratio method. Application to geological samples. *Talanta* **2002**, *58*, 811–821. [CrossRef]
40. Barnes, M.; Sulé-Suso, J.; Millett, J.; Roach, P. Fourier transform infrared spectroscopy as a non-destructive method for analysing herbarium specimens. *Biol. Lett.* **2023**, *19*, 20220546. [CrossRef]
41. Kassem, A.; Abbas, L.; Coutinho, O.; Opara, S.; Najaf, H.; Kasperek, D.; Pokhrel, K.; Li, X.; Tiquia-Arashiro, S. Applications of Fourier Transform-Infrared spectroscopy in microbial cell biology and environmental microbiology: Advances, challenges, and future perspectives. *Front. Microbiol.* **2023**, *14*, 1304081.
42. Zhang, S.; Song, J.; Du, Q.; Cheng, K.; Yang, F. Analog synthesis of artificial humic substances for efficient removal of mercury. *Chemosphere* **2020**, *250*, 126606. [CrossRef]
43. Yang, H.; Luo, B.; Zhang, Y.; Zhou, B.; Manzoor Ahmed, S.; Liu, H.; Liu, X.; He, Y.; Xia, S. Study of Humic Acid Adsorption Character on Natural Maifan Stone: Characterization, Kinetics, Adsorption Isotherm, and Thermodynamics. *ACS Omega* **2020**, *5*, 7683–7692. [CrossRef] [PubMed]
44. Cui, K.; Zhou, A.; Yu, C.; Jin, S. Investigation into the impact of Mn^{2+} and its interaction with calcite in the flotation of rhodochrosite. *Sep. Purif. Technol.* **2025**, *354*, 129312. [CrossRef]
45. Krishna Kanamarlapudi, S.L.R.; Muddada, S. Structural Changes of *Bacillus subtilis* Biomass on Biosorption of Iron (II) from Aqueous Solutions: Isotherm and Kinetic Studies. *Pol. J. Microbiol.* **2019**, *68*, 549–558. [CrossRef]
46. Azulay, D.N.; Spaeker, O.; Ghrayeb, M.; Wilsch-Bräuninger, M.; Scoppola, E.; Burghammer, M.; Zizak, I.; Bertinetti, L.; Politi, Y.; Chai, L. Multiscale X-ray study of *Bacillus subtilis* biofilms reveals interlinked structural hierarchy and elemental heterogeneity. *Proc. Natl. Acad. Sci. USA* **2022**, *119*, e2118107119. [CrossRef]
47. Tohry, A.; Dehghan, R.; Zarei, M.; Chelgani, S.C. Mechanism of humic acid adsorption as a flotation separation depressant on the complex silicates and hematite. *Miner. Eng.* **2021**, *162*, 106736. [CrossRef]
48. Dong, W.; Wang, H.; Ning, Z.; Hu, K.; Luo, X. Bioadsorption of Terbium(III) by Spores of *Bacillus subtilis*. *Minerals* **2022**, *12*, 866. [CrossRef]
49. Pourahmad, H.; Haddad, M.; Claveau-Mallet, D.; Barbeau, B. Impact of media coating on simultaneous manganese removal and remineralization of soft water via calcite contactor. *Water Res.* **2019**, *161*, 601–609. [CrossRef]

50. Terbouche, A.; Ramdane-Terbouche, C.A.; Hauchard, D.; Djebbar, S. Evaluation of adsorption capacities of humic acids extracted from Algerian soil on polyaniline for application to remove pollutants such as Cd(II), Zn(II) and Ni(II) and characterization with cavity microelectrode. *J. Environ. Sci.* **2011**, *23*, 1095–1103. [CrossRef]
51. Sounthararajah, D.P.; Loganathan, P.; Kandasamy, J.; Vigneswaran, S. Effects of Humic Acid and Suspended Solids on the Removal of Heavy Metals from Water by Adsorption onto Granular Activated Carbon. *Int. J. Environ. Res. Public. Health* **2015**, *12*, 10475–10489. [CrossRef] [PubMed]
52. Wróbel, M.; Śliwakowski, W.; Kowalczyk, P.; Kramkowski, K.; Dobrzyński, J. Bioremediation of Heavy Metals by the Genus Bacillus. *Int. J. Environ. Res. Public. Health* **2023**, *20*, 4964. [CrossRef]
53. Al-Harby, N.F.; Albahly, E.F.; Mohamed, N.A. Kinetics, Isotherm and Thermodynamic Studies for Efficient Adsorption of Congo Red Dye from Aqueous Solution onto Novel Cyanoguanidine-Modified Chitosan Adsorbent. *Polymers* **2021**, *13*, 4446. [CrossRef]
54. Musah, M.; Azeh, Y.; Mathew, J.T.; Umar, M.T.; Abdulhamid, Z.; Muhammad, A.I. Adsorption kinetics and isotherm models: A review. *CaJoST* **2022**, *4*, 20–26. [CrossRef]
55. Azizian, S.; Eris, S. Adsorption isotherms and kinetics. In *Interface Science and Technology*; Elsevier: Amsterdam, The Netherlands, 2021; Volume 33, pp. 445–509.
56. Wang, D.; Chen, H.; Xin, C.; Yuan, Y.; Sun, Q.; Cao, C.; Chao, H.; Wu, T.; Zheng, S. Insight into adsorption of Pb (II) with wild resistant bacteria TJ6 immobilized on biochar composite: Roles of bacterial cell and biochar. *Sep. Purif. Technol.* **2024**, *331*, 125660. [CrossRef]
57. Altowayti, W.A.H.; Salem, A.A.; Al-Fakih, A.M.; Bafaqeer, A.; Shahir, S.; Tajarudin, H.A. Optimization of as (V) removal by dried bacterial biomass: Nonlinear and linear regression analysis for isotherm and kinetic modelling. *Metals* **2022**, *12*, 1664. [CrossRef]
58. Volesky, B. Biosorption and me. *Water Res.* **2007**, *41*, 4017–4029. [CrossRef]
59. D'Anna, M.; Lubini, P.; Fuchs, H.U.; Corni, F. A Direct Entropic Approach to the Thermal Balance of Spontaneous Chemical Reactions. *Entropy* **2024**, *26*, 450. [CrossRef]